minerals

MDPI

Article

First Occurrence, Morphology, and Crystal-Chemistry of Carcinogenic Fibrous Erionite from the Vulsini Volcanic District (Central Italy)

Michele Mattioli [1,*], Matteo Giordani [1], Annarita Poetini [1] and Laura Valentini [2]

[1] Department of Pure and Applied Sciences, University of Urbino Carlo Bo, 61029 Urbino, Italy; matteo.giordani@uniurb.it (M.G.); a.poetini@campus.uniurb.it (A.P.)
[2] Department of Biomolecular Sciences, University of Urbino Carlo Bo, 61029 Urbino, Italy; laura.valentini@uniurb.it
* Correspondence: michele.mattioli@uniurb.it

Abstract

This study presents new morphological, mineralogical, and chemical data on fibrous erionite, a carcinogenic zeolite, discovered for the first time in the volcanic rocks of the Vulsini Volcanic District, Italy. The erionite fibers were investigated using OM, TGA, SEM-EDS, XRPD, and EDXRF techniques. They occur as inhalable aggregates composed of extremely thin, tangled crystals with very high aspect ratios, features that may enhance both inhalability and toxicological significance. Mineralogical associations with saponite indicate formation under low-temperature hydrothermal conditions (<150 °C), likely related to late- to post-magmatic fluid circulation through cavities and vesicles in the host volcanic rocks. Chemical analyses identify the zeolite as erionite-K, reflecting the potassic character of associated volcanic lithologies and highlighting the influence of host-rock and fluid chemistry on zeolite formation. Trace-element contents, particularly in As, V, Rb, and Pb, may represent an additional factor influencing fiber toxicity through synergistic effects. The occurrence of carcinogenic fibrous erionite in volcanic lithologies widely exploited for quarrying and industrial applications raises significant environmental and occupational health concerns for zeolitized volcanic terrains in central Italy. These findings highlight the need for detailed fiber characterization and mineralogical investigations to support exposure prevention and environmental risk assessment in future excavation and quarrying activities.

Keywords: zeolites; erionite; fiber morphology; Vulsini; potential health risk

Check for updates

Academic Editor: Andrey G. Kalinichev

Received: 15 May 2026
Revised: 11 July 2026
Accepted: 12 July 2026
Published: 14 July 2026

Copyright: © 2026 by the authors. Licensee MDPI, Basel, Switzerland. This article is an open access article distributed under the terms and conditions of the Creative Commons Attribution (CC BY) license.

1. Introduction

Decades of research on the toxicity and carcinogenicity of asbestos minerals have shown that inhaling fibrous particles that meet the dimensional criteria established by the World Health Organization (WHO) poses significant health risks. Such exposure may lead to chronic lung disease and cancer, particularly mesothelioma [1–9].

Although international regulatory frameworks [10] recognize the hazard associated with six asbestiform minerals (chrysotile and the amphiboles actinolite, anthophyllite, amosite, crocidolite, and tremolite), a wide range of fibrous mineral phases remains unregulated. Many of these exhibit toxicity and biopersistence levels comparable to, or even exceeding, those of regulated minerals [11]. These include other amphiboles, mineral species with chemical compositions similar to asbestos, and additional fibrous minerals,

such as zeolites. While most naturally occurring zeolites are non-fibrous, in many cases, some zeolites, such as clinoptilolite, edingtonite, erionite, ferrierite, gonnardite, dachiardite, kalborsite, mesolite, mordenite, natrolite, offretite, paranatrolite, scolecite, and thomsonite, can grow with acicular to strongly fibrous habit [12–16]. In this context, fibrous zeolites have emerged as a class of growing environmental and toxicological concern. Beyond erionite, the only fibrous zeolite currently regulated, recent mineralogical and toxicological studies have expanded attention to other fibrous zeolites, including offretite, ferrierite, and mordenite, revealing complex relationships between zeolites and toxicity [17–21].

Fibrous zeolites typically form through secondary crystallization processes. These processes occur within microcavities (e.g., vesicles or amygdales) in basic to intermediate volcanic rocks, or as a result of the diagenetic alteration of glassy pyroclastic deposits in confined lacustrine basins [22–24]. In both settings, zeolite formation is strongly controlled by the circulation of low-temperature hydrothermal fluids or alkaline meteoric waters, which promote dissolution of the host rock's glass matrix followed by precipitation of zeolitic phases [25–28]. The resulting morphology and composition of these zeolites are governed by factors such as fluid-rock interaction, permeability, and the availability of extra-framework cations [29,30].

The combination of fibrous morphology, high surface area, and cation-exchange capacity makes these minerals highly reactive not only in geological settings but also in biological environments, where they can promote the generation of reactive oxygen species [6,16,18–20,31–37]. Among them, erionite is the most toxicologically significant species and is classified by the International Agency for Research on Cancer as a Group 1 human carcinogen [10]. Its pathogenicity is closely linked to physicochemical properties, including a high aspect ratio, high surface area, and pronounced cation-exchange capacity. Recent studies [38,39] indicate that erionite may exhibit cytotoxicity exceeding that of crocidolite (blue asbestos). This increased toxicity is attributed to the ability of asbestos fibers to generate reactive oxygen species at the cell surface, thereby causing persistent oxidative stress, chronic inflammation, and DNA damage that may ultimately lead to neoplastic transformation [18]. The environmental and health significance of erionite has been documented worldwide. The associated risk was dramatically highlighted by a well-known epidemiological study conducted in Anatolia (Turkey), particularly in the villages of Karain and Tuzköy [40–42]. In these areas, the use of erionite-bearing zeolitized tuff as a construction material has resulted in an exceptionally high incidence of malignant mesothelioma, accompanied by elevated mortality rates within the local population [43–49]. These epidemiological observations have been corroborated by detailed mineralogical and crystallographic investigations aimed at elucidating the structure-toxicity relationships of erionite fibers [50]. Another notable case is reported in North Dakota (USA), where the use of erionite-bearing gravels for road surfacing has raised significant public health concerns [51]. Additional cases of mesothelioma potentially linked to erionite exposure have been documented in Mexico, New Zealand, and Iran [51–56].

In Italy, previous studies have documented the occurrence of erionite in limited areas, including Sardinia [57,58] and the Veneto Volcanic Province, northern Italy [30,59–61]. More recently, a new confirmed identification of erionite has been reported in volcanic rocks of Vico Volcano, central Italy, where it occurs primarily within microcavities in lavas and pyroclastic deposits [62]. Its formation is attributed to the circulation of late-stage hydrothermal fluids, suggesting that erionite may also be present in other comparable volcanic settings.

This study reports a new occurrence of erionite within the pyroclastic succession of the Vulsini Volcanic District (central Italy), characterized by a highly fibrous morphology. This distinctive habit provides new insights into the morphological variability of fibrous zeolites,

particularly erionite. A multi-analytical approach, comprising optical microscopy (OM), thermogravimetric analysis (TGA), scanning electron microscopy with energy-dispersive system (SEM-EDS), X-ray powder diffraction (XRPD), and energy dispersive X-ray fluorescence (EDXRF), was employed to characterize the material's morphological, chemical, and mineralogical features, and to assess their potential implications for environmental exposure and human health.

2. Erionite Background

Erionite belongs to the zeolite family, a group of tectosilicates characterized by an open, three-dimensional framework of TO4 tetrahedra (T = Si, Al), in which each oxygen atom is shared between two tetrahedral sites. The spatial arrangement of these units gives rise to a complex system of interconnected channels and cages at the molecular scale [22,63,64]. These structural features enable the incorporation of water molecules and extra-framework cations and confer a high cation-exchange capacity, which is central to their chemical reactivity. Isomorphic substitution of Si^{4+} by Al^{3+} within the framework generates a net negative charge, which is balanced by extra-framework cations (e.g., Na^+, Ca^{2+}, K^+) and associated hydration water molecules residing within the structural voids [50,63,65].

Erionite is a member of the ABC-6 structural family [63]. It crystallizes in the hexagonal system (space group $P6_3/mmc$), with unit-cell parameters of approximately a = 13.19–13.34 Å and c = 15.04–15.22 Å [15,66–71]. Its average chemical formula is $Na_2K_2Ca_3[Al_{10}Si_{26}O_{72}]\cdot 30H_2O$. Erionite was originally described as a single mineral species [22,72,73]. It is now classified as a mineral series due to its significant chemical variability, comprising three species (erionite-K, erionite-Ca, and erionite-Na) defined by the dominant extra-framework cation [49,65,74,75]. Erionite is often misidentified as offretite, a closely related zeolite with similar physical, chemical, and structural properties and the potential for intergrowth within a single crystal [70,76]. The most reliable distinction between the two species is based on the Mg/(Ca + Na) cation ratio.

Based on current knowledge, as summarized in a recent article [77], erionite can occur in different morphological forms that can be grouped into two main types: an extremely fibrous, hair-like ("woolly") form and acicular to prismatic crystals with rigid behavior ("prismatic").

"Woolly" erionite was first identified at the type locality near Durkee, Oregon (USA), by Eakle [78], who described it as follows: "zeolite occurs as very fine threads, having a snow-white color and pearly luster. These threads resemble fine woolly hairs, having the same curly nature and soft feel." This distinctive appearance gave rise to the mineral's name, derived from the Greek word for wool. This morphological type, also reported by several authors [19,30,36,56,57,61,62,68,79], is characterized by an extremely fibrous habit, consisting of hair-like fibers with diameters of 0.5–3 μm and highly variable lengths ranging from 200 to 300 μm. The longer fibers are tensile, elastic, and flexible and are composed of very thin, curled fibrils that may be as small as 10–15 nm. The fibers and fibrils commonly occur in sub-parallel or bent bundles that may ravel and fray into aggregates ranging from 2 to 10 μm in diameter. Erionite with a similar fibrous habit has also been reported to grow perpendicular to levyne surfaces, forming a characteristic erionite-levyne-erionite sequence that may be repeated to produce a "sandwich-like" structure.

"Prismatic" erionite commonly occurs as single acicular or elongated prismatic crystals and has been reported by several authors [20,30,33,50,52,54,61,62]. Individual acicular crystals are typically 5–10 μm in diameter and 100–500 μm in length, and may exhibit well-defined hexagonal cross sections at their terminations. Under the petrographic microscope, this type of erionite often appears as single acicular crystals; however, scanning electron microscopy reveals that these apparently "single" crystals are actually bundles of prismatic

crystals approximately 10–50 μm in diameter. Prismatic erionite may also occur as prisms of varying sizes, with diameters of ~250–600 μm and lengths of ~600–800 μm [20,61]. These prisms commonly show extensive fragmentation, producing fibrils ranging from <3 μm to ~50 μm in diameter and from <10 μm to ~100 μm in length. Erionite also forms radial aggregates or spherulites, ranging from ~50 μm to 1 mm in size, in which the hexagonal symmetry of individual crystals remains recognizable. Less commonly, it occurs as stubby bundles 5–80 μm long, each composed of tens to hundreds of crystals. In this type, crystals may appear solid and rigid, without evident fibrous features, or may split into numerous fibrils with rigid behavior and diameters consistently below ~1 μm, which can become partially or completely detached from the main crystal.

The morphology of erionite is strongly controlled by crystallization conditions, including temperature, fluid composition, supersaturation, and host-rock properties [15,22,24,63,67]. These factors influence nucleation and crystal growth, resulting in morphologies ranging from type 1 to type 2. Type 1 erionite, characterized by highly fibrous to woolly aggregates of often locally disordered fibers, is typically associated with rapid growth and high supersaturation. Under different conditions, erionite develops type 2 morphologies, forming acicular to prismatic crystals within vesicles or cavities of volcanic rocks. These may occur as isolated individuals, parallel intergrowths, or radiating and spherulitic aggregates formed by outward growth from nucleation points, reflecting more stable and organized crystallization regimes. The transition between these habits remains debated and is likely related to growth kinetics and structural defects [15].

3. Geological Framework

Magmatic rocks exposed along the Tyrrhenian margin of central Italy belong to four volcanic districts: Vulsini, Cimino, Vicano, and Sabatini (Figure 1). These districts are part of the Tuscan-Lazio volcanic province, which developed in a structurally depressed belt located between the Apennine chain and the Tyrrhenian coast, along the margin of the Tyrrhenian basin [80,81]. Volcanic rocks in this region range from acidic to intermediate in composition and are derived from both potassic and ultrapotassic magmas. Hybrid compositions are characteristic of the Cimino district, whereas the Vulsini, Vicano, and Sabatini districts are part of the Roman Comagmatic Province and are dominated by potassium-rich rocks [82–84].

The Vulsini Volcanic District is the northernmost and largest sector of the Roman Province, covering an area of approximately 2200 km^2. Its deposits are radially distributed around the volcano-tectonic depression now occupied by Bolsena Lake (Figure 1). Volcanic activity in the Vulsini District occurred between ~576 and 127 ka and involved five main volcanic complexes: Paleobolsena, Bolsena, Montefiascone, Latera, and Neobolsena, whose products partly overlap in space and time [85–88]. The earliest phase of activity (Paleobolsena) was characterized by plinian eruptions and pyroclastic flows (“basal ignimbrites”), which led to caldera collapse in the northern sector of present-day Bolsena Lake. Volcanic activity subsequently intensified in the northeastern sector, producing major eruptions such as the Orvieto–Bagnoregio Ignimbrite. Explosive activity then shifted first to the southeastern area (Montefiascone complex) and later to the western sector (Latera complex), where highly explosive eruptions generated numerous pyroclastic flows and triggered further caldera collapse. The final stage (Neobolsena) consisted of smaller-scale explosive and effusive eruptions from monogenetic centers, including scoria cones, tuff rings, and tuff cones.

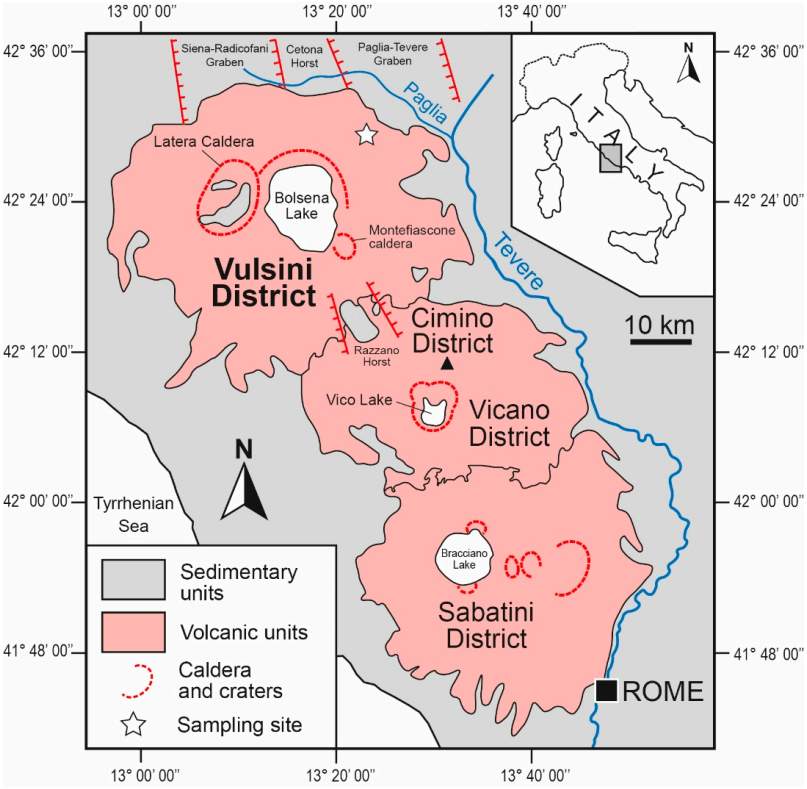

Figure 1. Geological sketch map of Central Italy showing the locations of the Vulsini, Cimino, Vicano, and Sabatini Volcanic Districts. The star indicates the sampling site (Porano quarry).

In the volcanic rocks of central Italy (mainly Vulsini, but also Vico and Cimini), several studies have documented widespread secondary mineralization processes and/or replacement of the glassy matrix in trachytic and phonolitic ignimbrites by phillipsite and chabazite, consistent with experimental predictions [26,28,29,89–91]. These studies also highlight the importance of "geoautoclave" conditions, in which thick, low-permeability pyroclastic deposits retain heat and fluids for long periods, allowing extensive zeolitization. Despite these advances, the understanding of post-emplacement zeolitization in these rock types is still incomplete. Several factors influence the distribution of zeolite species, including magma composition, cooling rate, deposit permeability, and fluid chemistry. As a result, the volcanoes of central Italy, where magma chemistry and eruptive mechanisms vary widely, show diverse zeolitization processes and authigenic mineral phases. This variability reflects the eruption of magmas belonging to different magmatic series within the same or nearby areas, ranging from acidic to intermediate compositions and including shoshonitic, alkaline potassic, and ultrapotassic rocks. In addition, chemical heterogeneity within a single ignimbrite layer can produce different zeolite assemblages both laterally and vertically. Therefore, detailed mineralogical and textural analyses are essential for reconstructing alteration histories and predicting the distribution of zeolites within pyroclastic deposits.

4. Materials and Methods

4.1. Materials

The investigated samples were collected from an inactive quarry exposing volcanic deposits (42°41′08″ N, 12°05′15″ E; Figure 1) in the municipality of Porano (southern Umbria, Porano, Italy). This area is characterized by a volcanic succession of pyroclastic fall and flow deposits attributed to the activity of the Vulsini Volcanic District. This succession comprises alternating pumice beds, pumice- and scoria-rich layers, compact, poorly sorted,

and poorly graded micropumice-rich beds, reddish ash horizons, lithified ash layers, and accretionary lapilli ash layers. These deposits are locally separated by erosional surfaces or paleosols, marking pauses in eruptive activity.

A representative set of pumice clasts, approximately 5 cm × 10 cm in size, was collected from the quarry area (see Section 5.1, "Field data", for a more detailed description). The secondary minerals occurring on the surfaces and within the cavities and vesicles of each pumice clast were then gently extracted, examined under a binocular microscope, and carefully cleaned to remove any adhering phases or other impurities. This procedure provided sufficiently pure material for subsequent mineralogical and chemical analyses.

4.2. Scanning Electron Microscopy (SEM-EDS)

The morphological and physical properties were examined using a Wild M10 binocular optical microscope (Leica Microsystems, Wetzlar, Germany) equipped with IntraLux 5000–1 illumination (Volpi AG, Dietikon, Switzerland) and a DCM-510 digital system.

Detailed morphological observations were carried out using an FEI Quanta 200 FEG environmental scanning electron microscope (ESEM; Hillsboro, OR, USA), equipped with an energy dispersive X-ray spectrometer (EDAX Inc., Mahwah, NJ, USA) and a spectrometric unit with an ECON (Edax Carbon Oxygen Nitrogen) 6 utw X-ray detector coupled with a Genesis Analysis software, 5.1 version, for semi-quantitative microchemical analysis. Analyses were performed on both isolated minerals and the internal surfaces of cavities and vesicles. In some cases, the samples were coated with gold to ensure electrical conductivity. Operating conditions included an accelerating voltage of 25 kV, variable beam diameter, a working distance of 10–12 mm, and a tilt angle of 0°. Additional observations have been carried out using a JEOL JSM-200 IT SEM (JEOL Ltd., Tokyo, Japan) with 10 to 30 kV of accelerating voltage, variable beam current, and a working distance of 10 mm, equipped with both an Everhart-Thornley type secondary electron detector and a high sensitivity, multi-element, solid state backscatter electron (BSE) detector.

Microchemical data were obtained using a JEOL 6400 SEM (JEOL Ltd., Tokyo, Japan) equipped with an Oxford Linkisis EDS system. Operating conditions were 15 kV accelerating voltage, 1.2 nA beam current, 10 mm working distance, 0° tilt angle, and a counting time of 60 s. Natural and synthetic standards were used for calibration. The reliability of the chemical analysis was assessed using the charge balance error formula E% [76,92], as well as Mg- and K-content tests [49,68,74]. For zeolites, analytical data are considered reliable when the charge balance error (E%) is within ±10%.

4.3. Thermogravimetric Analysis (TGA)

Thermogravimetric analysis (TGA) was performed using a TGA 400 (PerkinElmer, Waltham, MA, USA). The sample was heated from 30 to 800 °C at a rate of 10 °C/min under a nitrogen flow.

4.4. X-Ray Powder Diffraction (XRPD)

XRPD data were collected using a Philips X'Change PW1830 diffractometer (Panalytical, Amsterdam, The Netherlands) operating at 35 kV and 30 mA with CuKα radiation (λ = 1.54506 Å). From a particularly pure sample, the whitish fibrous portion was carefully isolated and checked, taking care to exclude impurities, in order to obtain fractions as pure as possible. Measurements were performed in Bragg–Brentano geometry over a 2θ range of 2° to 65°, with a step size of 0.01° and a counting time of 2.5 s per step to obtain high-intensity diffraction patterns. The instrument was equipped with a 1° divergence slit, a 0.2 mm receiving slit, and a graphite monochromator. Quantitative phase analysis was carried out using the reference intensity ratio (RIR) method with X'Pert Quantify and

X'Pert HighScore Plus software (version 5.2), using the PDF-4 database and quartz as an internal standard. Peak width variation remained within ±2% of the average value.

The sample was measured three times, showing highly reproducible results with minimal variation in peak positions and intensities.

4.5. Energy Dispersive X-Ray Fluorescence (EDXRF)

The same sample analyzed by XRPD was subsequently subjected to EDXRF chemical analysis to (1) verify the compositions obtained by microanalysis and (2) detect the possible presence of trace elements. Energy dispersive X-ray fluorescence analysis was performed using an Epsilon 1 instrument (Malvern Panalytical, Amsterdam, The Netherlands), equipped with a silver anode X-ray tube and a silicon drift detector (SDD) with an energy resolution of <135 eV (Mn-Kα). The sample was analyzed under two conditions. The first was optimized for low-atomic-number elements (Mg to Ca) at 10 kV, 500 μA, and an acquisition time of 180 s. The second targeted higher atomic number elements (V to Zr and Pb), using 50 kV, 100 μA, a 300 s acquisition time, and a 500 μm Cu filter. Quantitative analyses were carried out using the instrument's proprietary software, and each sample was measured three times. To assess precision and accuracy, an internal reference standard was analyzed under the same conditions as the sample. All measurements were performed at room temperature under atmospheric conditions. The reference sample was prepared to ensure a flat surface and complete irradiation during analysis, and spectra were processed using the instrument's software (Epsilon dashboard).

5. Results

5.1. Field Data

The inactive Porano quarry is characterized by a pyroclastic sequence (Figure 2) consisting, from bottom to top, of a compact fine-ash layer approximately 90 cm thick (Unit A), overlain by a thick pyroclastic flow deposit approximately 3 m thick (Unit B), which is, in turn, overlain by a second pyroclastic flow deposit (Unit C). Unit C consists of large, dark pumice clasts embedded in a fine-grained, brownish matrix and has a minimum thickness of approximately 1 m.

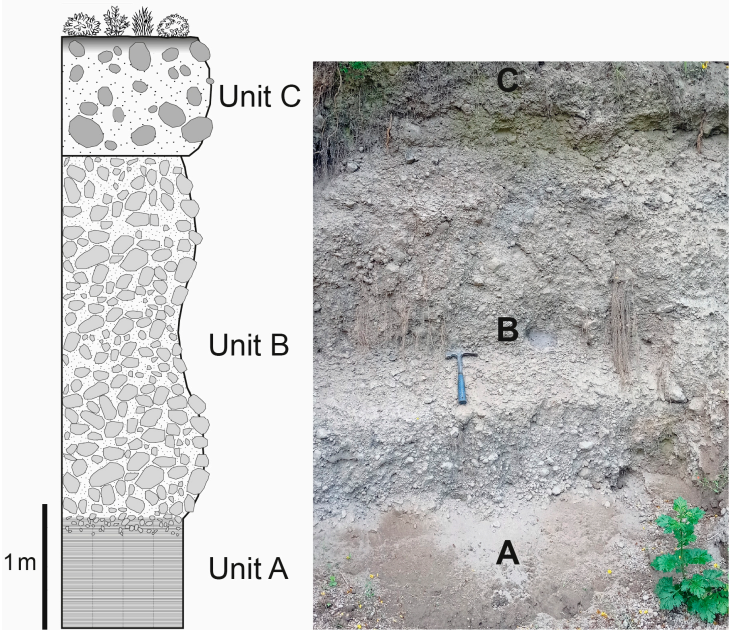

Figure 2. Representative stratigraphic log of the pyroclastic sequence exposed in the inactive quarry of Porano. Investigated samples were collected from Unit B.

The material extracted from this quarry was derived mainly from Unit B. This deposit is generally massive and medium- to poorly sorted, with sporadic lithic enrichment at its base. The dominant juvenile component (i.e., derived from the magma involved in the eruption) consists of angular gray pumice clasts ranging from a few centimeters to 30–40 cm in diameter, embedded in a fine-grained ash matrix containing rare centimeter-sized lithic fragments and darker juvenile components. Locally, spatter clasts and fragments occur in the lower part of the deposit. In places, the central and uppermost parts of the unit display stratification defined by matrix-rich layers. Conversely, the basal part of Unit B may contain a higher abundance of pumice lapilli at the expense of the ash matrix. The juvenile pumice clasts are vesiculated and display a heterogeneous texture, with a microcrystalline to cryptocrystalline groundmass containing poorly to moderately sorted components of varying sizes. The pumices are characterized by a highly porous, vesicular texture, with sub-spherical to irregular vesicles ranging in size from less than 1 mm to about 10 mm in diameter. Its color ranges from light gray to dark brownish-gray.

A notable feature of the juvenile pumice clasts in Unit B is the presence of erionite and clay minerals as secondary mineral phases, occurring both on clast surfaces and within vesicles and cavities (Figure 3). Three main morphological types of erionite were identified: (i) translucent, whitish patinas with bluish reflections, forming small, irregular, soft-looking clusters (Type 1, Figure 3B); (ii) delicate, soft, whitish or transparent films draping the surface like a veil (Type 2, Figure 3C); and (iii) whitish aggregates with a reticulated, fibrous texture that partially or completely fill vesicles and cavities, sometimes with spherulitic clay minerals (Type 3, Figure 3D).

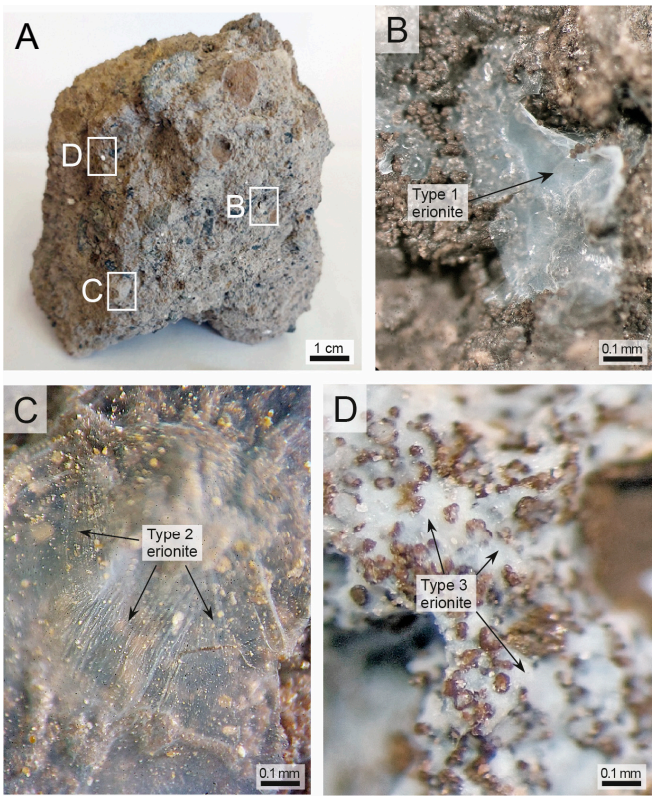

Figure 3. (**A**) Macroscopic appearance of a vesiculated juvenile pumice clast from Unit B of Porano quarry pyroclastic sequence, showing the three different morphological types of erionite occurrence. (**B**) Translucent, whitish-bluish patinas, forming small, irregular, soft-looking clusters (Type 1). (**C**) Delicate, soft, transparent films draping the surface like a veil (Type 2). (**D**) Close-up of a cavity lined with dense yet delicate, whitish aggregates displaying a reticulated, fibrous texture with spherulitic clay minerals (Type 3).

The degree of vesiculation and the extent of secondary mineral infill significantly vary among pumice clasts, with some showing more compact textures and others preserving a highly porous, open framework structure.

5.2. Morphological Data

From a macroscopic perspective (see Figure 3), scanning electron microscopy revealed additional morphological details for these three types.

Erionite of Type 1 (Figure 4), which appears as soft-looking clusters, consists of a superposition of very thin sheets, which may be either tightly compacted or loosely arranged with distinct separations between adjacent sheets. Each sheet is composed of a dense network of extremely fine erionite fibers (<0.1 μm in diameter) with variable lengths, forming a fabric-like texture. The fibers commonly show characteristic terminations, small tufts resembling paintbrush bristles.

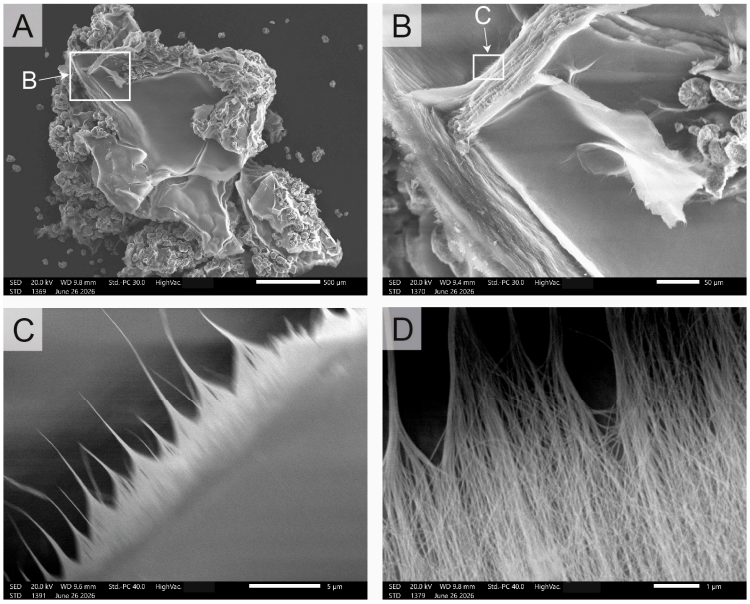

Figure 4. SEM images of Type 1 erionite. (**A**) General view of a soft-looking cluster. (**B**) Detail of panel (**A**), showing that the cluster consists of a stack of very thin sheets that may be either tightly compacted (left) or loosely arranged, with distinct separations between adjacent sheets (center and right). (**C**) Detail of panel B showing the characteristic terminations of fibers as small tufts resembling paintbrush bristles. (**D**) Higher-magnification view of a single sheet, revealing a dense network of extremely fine erionite fibers (<<0.1 μm in diameter).

Type 2 erionite (Figure 5), which appears as a transparent veil, consists of delicate, soft films that drape the surfaces. The film appears highly homogeneous. In areas where it exhibits undulations, it is seen to consist entirely of a network of extremely fine erionite fibers (<<0.1 μm in diameter), locally appearing stretched and broken. At higher magnification, the fibers are densely interwoven, producing a fabric-like texture.

Erionite of Type 3 (Figure 6), which appears as whitish aggregates, exhibits a characteristic nebulous, filamentous appearance, often resembling a soft, three-dimensional cloud of extremely thin, tangled fibers. At higher magnification, the fibers become clearly visible and are locally grouped into small bundles with "sheaf-like" morphologies. The length of these fibers is highly variable, but generally in the order of a few tens of microns. Their diameter, however, is extremely small (<<1 μm), indicating a high aspect ratio. The cloudy appearance is particularly evident when erionite forms above the spherulites that are often present as additional secondary minerals within cavities. At SEM magnification, the spherulites appear as fibrous, radial aggregates of very small crystals (a few microns

in size), exhibiting a highly lamellar and irregular morphology. Microchemical analysis indicates that these particles can be attributed to saponite (smectite group).

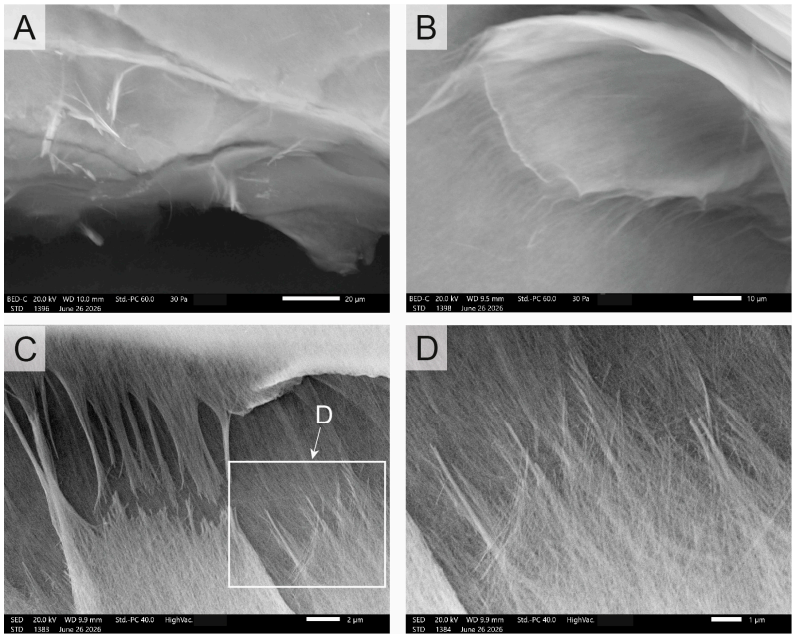

Figure 5. SEM images of Type 2 erionite. (**A**,**B**) General views of a delicate, soft film of erionite. (**C**) Detail of a curved area, showing extremely fine erionite fibers (<<0.1 µm in diameter) that locally appear stretched and broken. (**D**) Higher-magnification view of a portion of the film, showing densely interwoven fibers that produce a fabric-like texture.

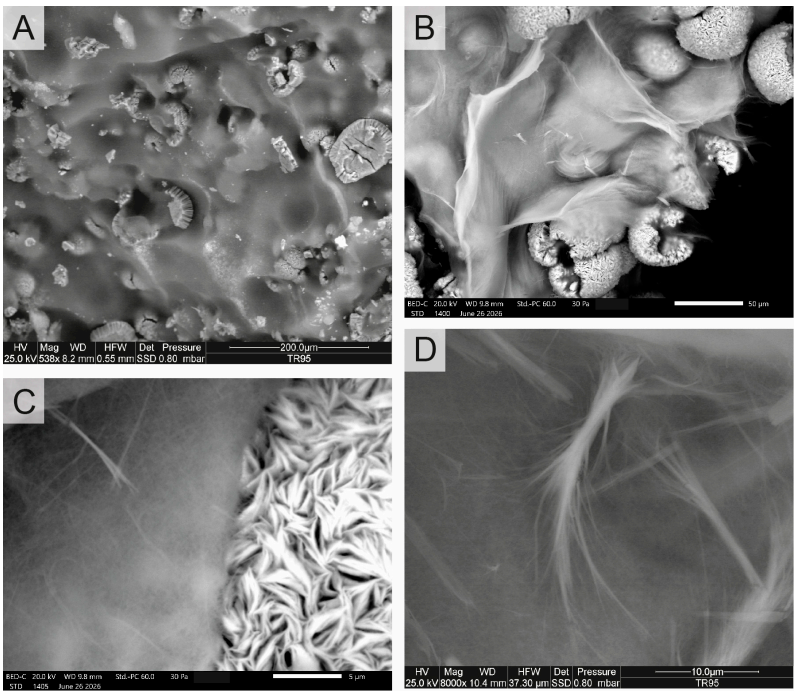

Figure 6. SEM images of type 3 erionite. (**A**) General view of a diffuse, hazy patina of fibrous erionite with sub-millimeter spherulites of saponite resting on or protruding from the surface. (**B**) Detail of the patina, showing a characteristic nebulous, filamentous appearance composed of extremely thin, tangled erionite fibers covering saponite spherules. (**C**) Close-up of the erionite coating on a saponite spherulite, showing the individual fibers that compose the patina. (**D**) The fibers are locally arranged into small bundles displaying characteristic sheaf-like morphologies.

5.3. Mineralogical Data

X-ray powder diffraction (XRPD) analysis was conducted on a particularly pure Type 1 erionite cluster (inset of Figure 7), which was carefully examined under a binocular microscope to verify the absence of impurities or other mineral phases. The resulting pattern (Figure 7) is characterized by a series of sharp, well-defined reflections, indicating a highly crystalline material dominated by a nearly pure zeolitic phase.

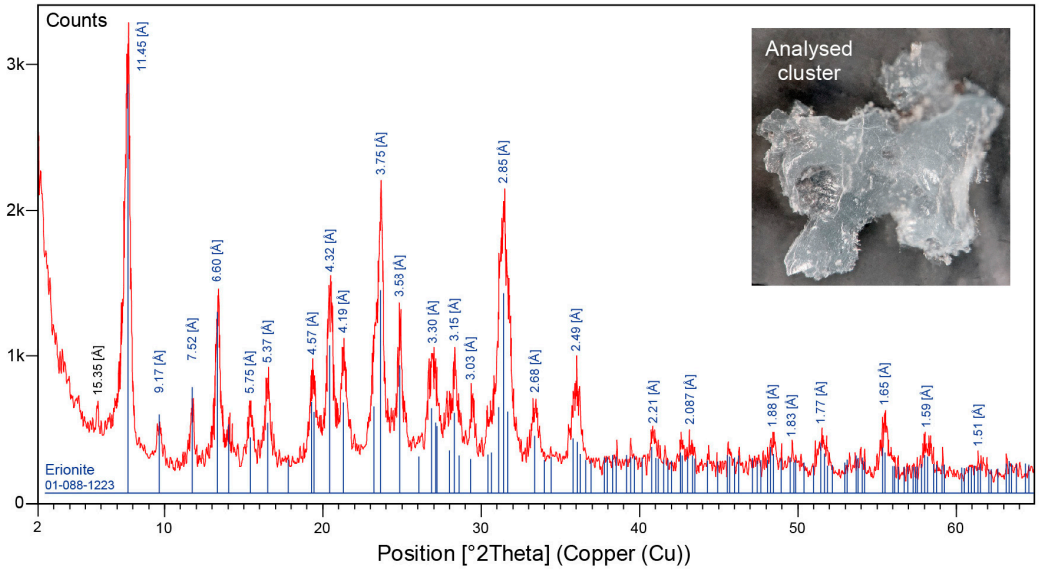

Figure 7. XRPD pattern of a soft cluster of an almost pure, fibrous erionite (see the inset). All reflections shown in blue are consistent with the erionite reference pattern, whereas the reflection shown in black is attributed to saponite impurities.

The strongest reflection occurs at a d-spacing ~11.45 Å, corresponding to the (100) plane (~7.7° 2θ), and representing a diagnostic low-angle reflection of erionite, in good agreement with the reference pattern. Additional characteristic reflections are observed at approximately 13.2° (d ≈ 6.60 Å), 20.5° (d ≈ 4.32 Å), 23.4° (d ≈ 3.75 Å), 25° (d ≈ 3.58 Å), and 31.5° 2θ (d ≈ 2.85 Å), consistent with the diagnostic peaks reported for erionite in the literature [38,70,76]. The positions of these reflections match the characteristic crystallographic features of the erionite-group minerals.

The strong correspondence between the experimental and reference patterns confirms that the fibrous fraction is dominated by erionite. The relative intensity of the low-angle peak and the sharpness of the reflections suggest a well-ordered crystalline structure, typical of fibrous zeolites with a high degree of structural organization. At low angles (≈5.7° 2θ), a weak reflection corresponding to a d-spacing of 15.35 Å is observed, likely associated with traces of saponite impurities (2%–3%) that remained incorporated in the extracted fibrous erionite fraction.

5.4. Thermogravimetric Data

The water content of the pure Type 1 erionite cluster was determined by thermogravimetric analysis (TGA). The TGA curve shows an initial major mass loss of 14.813% up to 560 °C, followed by a second, smaller mass loss of 3.672% between 560 °C and 670 °C, for a total mass loss of 18.485% (Figure 8). During the second stage, a small fraction of the water loss (not quantifiable) may also be associated with impurities.

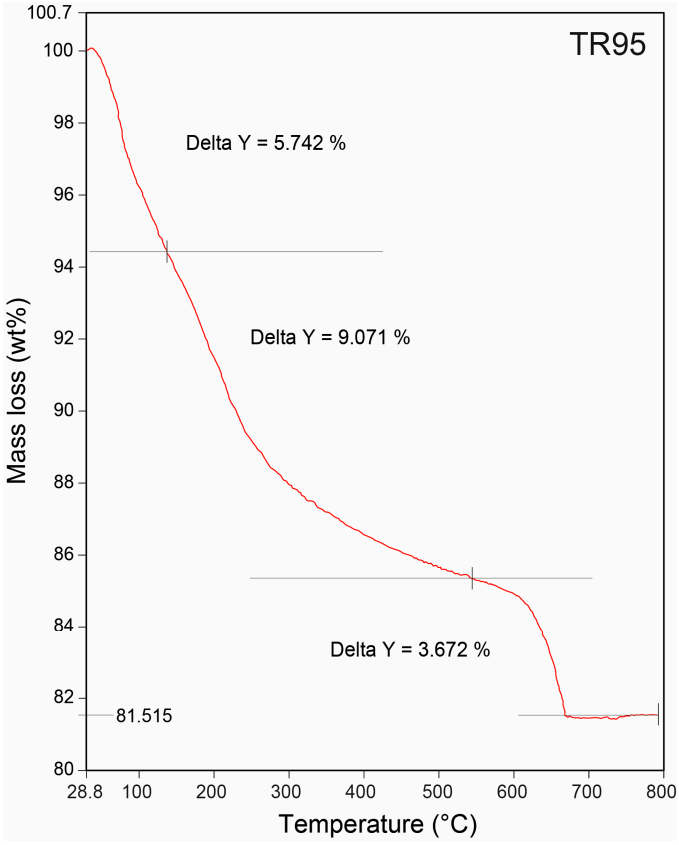

Figure 8. Thermogravimetric (TGA) curve of the pure Type 1 erionite cluster.

5.5. Chemical Data

The analyzed samples show a chemical composition (Table 1) consistent with that of erionite-K, as indicated by the dominance of K among the extra-framework cations. The calculated structural formula, normalized to 36 tetrahedral sites, yields ΣT values close to 72 apfu (atoms per formula unit) and is in good agreement with the idealized composition $K_2(Na,K,Ca_{0.5})_7[Al_9Si_{27}O_{72}]\cdot 30H_2O$ (Ref. [76]), indicating good internal consistency of the analytical data and a reliable representation of the tetrahedral framework. The Si/Al ratios range between ~3.3 and 3.5, in agreement with typical erionite compositions and indicating a relatively silica-rich framework [38,70,76,93].

The limited variability observed among the samples suggests a chemically homogeneous tetrahedral framework. Charge balance is achieved by extra-framework cations, mainly K, Ca, and Na, with minor Mg. Potassium is consistently the dominant cation (K ≈ 2.5–2.9 apfu), supporting the classification of the studied material as erionite-K [92,94]. Calcium and sodium show moderate variability, ranging from 1.68 to 1.96 apfu and 0.62 to 1.09 apfu, respectively. Magnesium content is very low (0.15 to 0.57 apfu), consistent with literature data for erionite. These values are also reflected in the Mg/(Ca + Na) ratio (0.05–0.23), which is considered fundamental for distinguishing between the closely related species erionite and offretite (erionite is characterized by a Mg/(Ca + Na) ratio < 0.3; [76]). Chemical analyses also reveal traces of iron (0.02–0.04 apfu). The calculated extra-framework cation population is consistent with the charge deficit generated by Al substitution in the tetrahedral framework, as also confirmed by generally low E% values (<10%).

Major (wt%) and trace elements concentrations (in ppm) from EDXRF analysis of the pure Type 1 erionite cluster are reported in Table 2.

Table 1. SEM-EDS chemical analyses of erionite from the different morphological types. Structural formulas are based on 72 oxygens and are calculated on an anhydrous basis. H_2O is calculated by TGA. Σ*T* represents the sum of the tetrahedral site, while Σ*ET* denotes the sum of the extra-tetrahedral site. E% as defined by Passaglia [92].

Sample	TR95-1	TR95-2	TR95-3	TR95-4	TR95-5	TR95-6	TR95-7	TR95-8	TR95-9	TR95-10
SiO_2	57.53	57.75	57.57	58.01	58.00	57.44	57.90	58.03	57.70	57.77
Al_2O_3	14.42	14.13	14.60	14.28	14.40	14.78	14.49	14.63	14.37	14.14
Fe_2O_3	0.10	0.05	0.05	0.05	0.00	0.05	0.00	0.06	0.11	0.12
MgO	0.43	0.41	0.45	0.30	0.38	0.20	0.26	0.47	0.37	0.78
CaO	3.78	3.57	3.40	3.78	3.34	3.56	3.77	3.25	3.65	3.57
BaO	0.00	0.00	0.00	0.00	0.00	0.00	0.00	0.00	0.00	0.00
Na_2O	0.91	0.83	1.01	1.10	0.79	1.17	0.90	0.85	0.79	0.67
K_2O	4.29	4.51	4.45	4.15	4.79	4.24	4.30	4.37	4.01	4.23
H_2O	18.49	18.49	18.49	18.49	18.49	18.49	18.49	18.49	18.49	18.49
Total	99.95	99.74	100.01	100.17	100.18	99.92	100.10	100.16	99.48	99.77
apfu based on 72 oxygen atoms										
Si	27.80	27.97	27.80	27.93	27.95	27.75	27.89	27.89	27.94	27.91
Al	8.22	8.07	8.31	8.10	8.18	8.42	8.23	8.19	8.20	8.06
Fe^{2+}	0.04	0.02	0.02	0.02	0.00	0.02	0.00	0.02	0.04	0.04
ΣT	36.06	36.06	36.12	36.06	36.13	36.19	36.12	36.10	36.18	36.01
Mg	0.31	0.30	0.32	0.21	0.27	0.15	0.19	0.34	0.26	0.57
Ca	1.96	1.85	1.76	1.95	1.72	1.84	1.95	1.68	1.90	1.85
Ba	0.00	0.00	0.00	0.00	0.00	0.00	0.00	0.00	0.00	0.00
Na	0.86	0.78	0.95	1.02	0.73	1.09	0.84	0.80	0.74	0.62
K	2.64	2.78	2.74	2.55	2.94	2.61	2.64	2.68	2.48	2.60
H_2O	29.80	29.87	29.78	29.69	29.72	29.80	29.71	29.64	29.86	29.80
Σ non T sites	35.57	35.58	35.54	35.43	35.39	35.49	35.32	35.13	35.23	35.44
Total	71.62	71.64	71.66	71.49	71.52	71.68	71.44	71.23	71.41	71.45
E%	2.77	2.90	6.12	2.79	6.72	9.84	6.24	9.52	9.33	0.58

Table 2. Major (wt%) and trace elements concentrations (in ppm) of the pure Type 1 erionite cluster from EDXRF analysis. H_2O is calculated by TGA.

Major Elements (wt%)		Trace Elements (ppm)	
SiO_2	58.15	Pb	22.3
Al_2O_3	14.31	V	35.3
Fe_2O_3	0.15	Mn	44.8
MgO	0.56	Zn	9.77
CaO	3.62	As	48.1
Na_2O	0.76	Rb	45.6
K_2O	3.96	Sr	255
H_2O	18.49	Ba	364
Total	100		

Regarding major elements, the chemical composition is fully consistent with that determined by SEM-EDS microanalysis, confirming the reliability of the dataset. The following trace elements were measured: Sc, V, Cr, Mn, Co, Ni, Cu, Zn, As, Rb, Sr, Y, Sb, Cs, Ba, La, Pb, Ce, Pr, Nd, Sm, Eu, Gd, Tb, Dy, Ho, Er, Tm, Yb, Lu, Th, and U. Table 2 reports only the concentrations of the detected trace elements; elements below the detection limits are not reported. The highest concentrations are those of Sr and Ba (255 and 364 ppm, respectively), which are classified in geochemistry as Large-Ion Lithophile Elements (LILEs) and behave as low-field-strength cations. Elements such as Mn (44.8 ppm), V (35.3 ppm), As (48.1 ppm), and Rb (45.6 ppm) occur at lower but still significant concentrations, whereas Pb and Zn are present at even lower values (22.3 and 9.77 ppm, respectively).

6. Discussion

The present work documents the first occurrence of fibrous erionite in volcanic rocks from the Vulsini Volcanic District, central Italy, thereby extending the known distribution of this rare zeolite within the Roman Comagmatic Province. As noted in the Introduction, erionite is a naturally occurring fibrous zeolite that is highly hazardous, with a carcinogenic potential reported to be comparable to, or even higher than, that of some asbestos minerals. Classified as a Group 1 carcinogen by the International Agency for Research on Cancer (IARC) [10], it can cause malignant pleural mesothelioma when inhaled, as its fine fibers can penetrate deep into the lungs.

Awareness of a hazard is essential for effective risk mitigation. Therefore, understanding how this mineral occurs in nature is crucial for reducing exposure risk. To date, erionite has been described in two main morphological forms: an extremely fibrous, hair-like, flexible variety, and acicular to prismatic crystals with a more rigid habit (see Section 2). Compared with these forms, erionite from the Vulsini Volcanic District exhibits a distinctive habit at both macroscopic and microscopic scales. The investigated samples contain mineralized cavities coated by a whitish, diffuse, hazy material with a characteristic nebulous, filamentous appearance, often resembling a soft, three-dimensional cloud. This material, which cannot be resolved without a microscope, could easily be misinterpreted as being formed by other minerals (e.g., carbonates) or as the result of microbial growth (e.g., fungi and molds). However, SEM observations reveal that it consists of extremely thin, tangled fibers forming a soft, three-dimensional network. At higher magnification, the fiber diameters are extremely small, generally well below 1 μm. This morphology indicates a very high aspect ratio, a key feature in assessing the potential inhalability and biological relevance of mineral fibers [1,10,95].

Erionite forms under specific low-temperature diagenetic conditions. Its occurrence depends not only on fluid chemistry but also on the interaction between volcanic glass composition, depositional environment, and pore-fluid chemistry, which together promote the formation of fibrous erionite rather than other zeolites. Erionite is typically associated with alkaline, saline lake or closed-basin environments, low-temperature alteration, glass-rich volcanic deposits, restricted silica activity, and high alkalinity. Several of these conditions, including pumice-rich deposits, abundant volcanic glass, alkaline environments, and low-temperature alteration, are present in the study area. This new finding is particularly relevant in light of the recent identification of erionite in volcanic rocks from another sector of the Roman Comagmatic Province (Vico Volcano [62]), suggesting that erionite formation may not be an isolated phenomenon but rather a locally favored process within zeolitized volcanic products of central Italy. Compared with erionite from the Vico volcanic rocks, the Vulsini erionite shares several key features, including occurrence within volcanic cavities, fibrous habit, and a K-rich chemical signature. However, the characteristic morphology observed in the Vulsini samples appears particularly distinctive and may reflect specific local conditions during fiber nucleation and growth, such as cavity geometry, fluid composition, and the degree of alteration of the host volcanic rock. The occurrence of erionite in both Vico and Vulsini volcanic products suggests that fibrous zeolite formation may be locally favored in zeolitized volcanic units, which are affected by late- to post-magmatic fluid circulation.

The coexistence of fibrous erionite and radial aggregates of saponite is also mineralogically significant. Saponite, a trioctahedral smectite, commonly forms during low-temperature alteration of volcanic glass and/or mafic components under fluid-rich conditions [25,28,30]. In experiments on volcanite-seawater interaction, smectites (usually saponites) are commonly produced at temperatures <150 °C [96,97]. In several hydrothermal systems, di- and trioctahedral smectites transform at 200–240 °C into kaolinite–smectite

mixed layers and corrensite, which are the predominant layer silicates in the temperature range of 245–265 °C. At higher temperatures, chlorite is the most abundant clay mineral, with minor C/S mixed layers. Its close association with erionite, also indicative of low-temperature conditions, suggests that the fibrous aggregates formed during a broader alteration process at temperatures <150 °C that affected the volcanic host rock. The presence of both minerals within cavities and vesicles suggests the circulation of late- to post-magmatic fluids through open pore spaces, where zeolite and clay minerals could nucleate and grow. In similar contexts, alteration sequences can be reconstructed by identifying successive episodes of fluid infiltration and mineral precipitation, using mineral assemblages, textures, zoning patterns, and cross-cutting relationships as key evidence. However, at present, the available data are insufficient to support such a detailed reconstruction. The only indication emerging from the dataset is that saponite may represent either an early alteration product preceding erionite crystallization or a coeval phase formed under slightly different local physicochemical conditions.

The major-element chemical composition of the fibrous aggregates is consistent with erionite-K, as indicated by SEM-EDS microanalysis and supported by EDXRF data. The dominance of K among the extra-framework cations is consistent with the high-potassic signature of volcanic products from the Roman Comagmatic Province. This suggests that the chemistry of the host rocks and circulating fluids exerted an important control over the extra-framework cation population of the zeolite. The presence of iron, although in very low amounts, is also noteworthy because Fe is not expected to be a structural component of erionite and may instead be associated with minor impurities (i.e., saponite lamellae) or particles adhering to fiber surfaces [38].

The trace-element composition of the fibrous erionite must also be interpreted with caution. Mineral impurities are commonly reported in raw fibrous mineral samples, although generally in very minor amounts, and may contribute to the bulk trace-element budget [98,99]. In the present case, the only impurity associated with fibrous erionite is saponite. Therefore, small amounts of trace elements may be incorporated into the saponite crystal lattice and/or interlayer sites. However, the contribution of accessory phases is expected to be very limited, given the high purity of the separated fibrous fraction, as indicated by XRPD results. For this reason, we cannot exclude that some trace elements are intrinsic to the chemical composition of erionite itself. Furthermore, erionite and other zeolitic materials are well known for their high capacity to host and retain trace elements and have been investigated for the removal of toxic elements from contaminated waters and industrial wastewater [22,100,101]. In the studied samples, the significant amounts of Mn, As, V, Rb, and Pb suggest that the fibrous erionite-rich material may have interacted with trace-element-bearing fluids during or after mineral formation. The presence of As in fibrous erionite may be related to the affinity of zeolitic materials for As species; however, its exact location cannot be established from EDXRF data alone [98,102].

Although the trace-element data do not directly provide information on bioavailability, they remain relevant because the toxicological behavior of mineral fibers may depend not only on morphology and durability, but also on surface chemistry and associated chemical components [11,37,103]. The occurrence of potentially toxic trace elements such as As, V, Rb, and Pb is also relevant, as these elements have been associated with adverse respiratory outcomes and increased lung cancer risk following cumulative exposure. Therefore, the toxic potential of fibrous erionite may depend not only on fiber morphology and biopersistence, but also on the combined effects of trace elements hosted within the erionite-rich material or adsorbed onto fiber surfaces. However, this interpretation should be treated with caution, since the bioaccessibility, speciation, and actual biological availability of these trace elements were not directly investigated in this study.

Finally, an important issue related to human health must be emphasized. Although the presence of zeolites in the volcanic rocks of Latium is well known, the species reported so far are all non-fibrous zeolites, mainly chabazite and phillipsite. The discovery of fibrous erionite in lithologies that are extensively quarried and widely used, therefore, raises important concerns regarding risk assessment and occupational exposure. Although the quarry investigated in this study is currently inactive and does not pose an immediate exposure risk, the identification of fibrous erionite in the Vulsini volcanic rocks has important implications for environmental management. Any future reactivation of the quarry, new excavation activities, or exploitation of similar zeolitized volcanic deposits should be preceded by detailed mineralogical screening, including XRPD, SEM-EDS, and fiber-dimensional analysis. Therefore, this finding should be regarded not only as a mineralogical novelty but also as an early warning for future environmental and occupational risk assessments in zeolitized volcanic terrains of central Italy.

7. Conclusions

In this work, new morphological, mineralogical, and chemical data are presented for erionite from the Vulsini Volcanic District (central Italy), where this carcinogenic zeolite occurs as inhalable fibrous aggregates. The main conclusions are as follows:

- This study documents the first occurrence of carcinogenic fibrous erionite in volcanic rocks from the Vulsini District, extending the known distribution of this hazardous zeolite within the Roman Comagmatic Province.
- The identified erionite exhibits a distinctive morphology, consisting of transparent films composed of extremely thin, tangled fibers with very high aspect ratios, features that may enhance inhalability and toxicological relevance.
- The association of fibrous erionite with saponite indicates formation under low-temperature hydrothermal alteration conditions (<150 °C), likely related to late- to post-magmatic fluid circulation through cavities and vesicles in the volcanic host rocks.
- Chemical analyses confirm the occurrence of erionite-K. The dominance of K reflects the potassic character of the volcanic rocks from central Italy and highlights the influence of host-rock and fluid chemistry on zeolite composition.
- The presence of potentially toxic trace elements, such as As, V, Rb, and Pb, may represent an additional factor influencing fiber toxicity through possible synergistic effects, although this hypothesis requires further investigation.
- The occurrence of carcinogenic fibrous erionite in volcanic lithologies commonly subjected to quarrying and industrial use raises important environmental and occupational health concerns in zeolitized volcanic terrains of central Italy, emphasizing the need for detailed risk assessment studies.
- Future quarrying, excavation, or exploitation of similar volcanic deposits should therefore include detailed mineralogical and fiber-characterization investigations to support effective exposure prevention and environmental risk management.

Author Contributions: M.M.: supervision, conceptualization, methodology, investigation, data curation, writing—original draft preparation, writing—review and editing, and funding acquisition. M.G.: formal analysis, data curation, writing—review and editing. A.P.: writing—original draft preparation, data curation, writing—review and editing. L.V.: data curation, writing—review and editing. All authors have read and agreed to the published version of the manuscript.

Funding: This project is funded by the INAIL-BRIC 2022 project (grant number ID 71; CUP: B27G23000010005). Part of the research was conducted under the framework of the 2022 research programs of the Department of Pure and Applied Sciences of the University of Urbino Carlo Bo

(PROG2022 "New asbestiform natural fibers: mineralogical and physical-chemical characterization of fibrous zeolites", responsible author: M. Mattioli).

Data Availability Statement: The main data are contained within the article.

Acknowledgments: We warmly thank E. Salvioli Mariani for her kind assistance during the acquisition of the microchemical data and E. Macedi for valuable technical support during the TGA analyses. We sincerely thank both reviewers for their thoughtful comments and constructive suggestions, which have significantly improved the quality of the manuscript. During the preparation of this manuscript, the authors used ChatGPT 5.0 (developed by OpenAI) to improve the clarity and style of the scientific English and to identify and correct typographical and grammatical errors. The authors have reviewed and edited the output and take full responsibility for the content of this publication.

Conflicts of Interest: The authors declare no conflicts of interest. The funders had no role in the design of the study; in the collection, analysis, or interpretation of data; in the writing of the manuscript; or in the decision to publish the results.

References

1. Guthrie, G.D.; Mossman, B.T. Merging the geological and biological sciences: An integrated approach to the study of mineral-induced pulmonary diseases. *Rev. Mineral. Geochem.* **1993**, *28*, 1–10. [CrossRef]
2. Davis, J.M.G. The role of clearance and dissolution in determining the durability or biopersistence of mineral fibers. *Environ. Health Perspect.* **1994**, *102*, 113–117. [CrossRef] [PubMed]
3. Fubini, B.; Bolis, V.; Cavenago, A.; Volante, M. Physico-chemical properties of crystalline silica dusts and their possible implication in various biological responses. *Scand. J. Work Environ. Health* **1995**, *21*, 9–14. [PubMed]
4. Fubini, B. Use of physico-chemical and cell-free assays to evaluate the potential carcinogenicity of fibers. In *Mechanisms of Fiber Carcinogenesis*; Kane, A.B., Boffetta, P., Saracci, R., Wilbourn, J.D., Eds.; International Agency for Research on Cancer: Lyon, France, 1996; Volume 140, pp. 35–54.
5. Carbone, M.; Bedrossian, C.W.M. The pathogenesis of mesothelioma. *Semin. Diagn. Pathol.* **2006**, *23*, 56–60. [CrossRef] [PubMed]
6. Oberdörster, G.; Oberdörster, E.; Oberdörster, J. Nanotoxicology: An emerging discipline evolving from studies of ultrafine particles. *Environ. Health Perspect.* **2005**, *113*, 823–839. [CrossRef] [PubMed]
7. de Assis, L.V.M.; Locatelli, J.; Isoldi, M.C. The role of key genes and pathways involved in the tumorigenesis of malignant mesothelioma. *Biochim. Biophys. Acta.* **2014**, *1845*, 232–247. [CrossRef] [PubMed]
8. Nielsen, L.S.; Bælum, J.; Rasmussen, J.; Dahl, S.; Olsen, K.E.; Albin, M.; Hansen, N.C.; Sherson, D. Occupational Asbestos Exposure and Lung Cancer—A Systematic Review of the Literature. *Arch. Environ. Occup. Health* **2014**, *69*, 191–206. [CrossRef] [PubMed]
9. Metintaş, M.; Ak, G.; Metintaş, S. Environmental asbestos exposure and lung cancer. *Lung Cancer* **2024**, *194*, 107850. [CrossRef] [PubMed]
10. International Agency for Research on Cancer (IARC). Asbestos (chrysotile, amosite, crocidolite, tremolite, actinolite and anthophyllite). IARC Monographs on the evaluation of the carcinogenic risk to humans. *Arsen. Met. Fibers Dusts.* **2012**, *100*, 219–309.
11. Gualtieri, A.F. Towards a quantitative model to predict the toxicity/pathogenicity potential of mineral fibers. *Toxicol. Appl. Pharmacol.* **2018**, *361*, 89–98. [CrossRef] [PubMed]
12. Belitsky, I.A.; Zolotarev, A.A.; Pekov, I.V. Fibrous zeolites: Crystal chemistry and morphology. *Mineral. Mag.* **1992**, *56*, 301–312.
13. Thomas, K.; Ballantyne, B. The morphology and biological activity of mineral fibers. *Ann. Occup. Hyg.* **1992**, *36*, 1–19.
14. Artioli, G.; Galli, E. *Natural Zeolites*; Reviews in Mineralogy; Mineralogical Society of America: Washington, DC, USA, 1999.
15. Armbruster, T.; Gunter, M.E. Crystal structures of natural zeolites. In *Natural Zeolites: Occurrence, Properties, Applications*; Bish, D.L., Ming, D.W., Eds.; Reviews in Mineralogy and Geochemistry; Mineralogical Society of America and Geochemical Society: Washington, DC, USA, 2001; Volume 45, pp. 1–68.
16. Betti, M.; Nasoni, M.G.; Luchetti, F.; Giordani, M.; Mattioli, M. Potential Toxicity of Natural Fibrous Zeolites: In Vitro Study Using Jurkat and HT22 Cell Lines. *Minerals* **2022**, *12*, 988. [CrossRef]
17. Mattioli, M.; Giordani, M.; Arcangeli, P.; Valentini, L.; Boscardin, M.; Pacella, A.; Ballirano, P. Prismatic to asbestiform offretite from Northern Italy: Occurrence, morphology and crystal-chemistry of a new potentially hazardous zeolite. *Minerals* **2018**, *8*, 69. [CrossRef]
18. Giordani, M.; Ballirano, P.; Pacella, A.; Meli, M.A.; Roselli, C.; Di Lorenzo, F.; Fagiolino, I.; Mattioli, M. Another Potentially Hazardous Zeolite from Northern Italy: Fibrous Mordenite. *Minerals* **2022**, *12*, 627. [CrossRef]

19. Giordani, M.; Mattioli, M.; Cangiotti, M.; Fattori, A.; Ottaviani, M.F.; Betti, M.; Ballirano, P.; Pacella, A.; Di Giuseppe, D.; Scognamiglio, V.; et al. Characterisation of potentially toxic natural fibrous zeolites by means of electron paramagnetic resonance spectroscopy and morphological-mineralogical studies. *Chemosphere* **2022**, *291*, 132918. [CrossRef] [PubMed]
20. Giordani, M.; Nasoni, M.G.; Bargagni, E.; Cangiotti, M.; Luchetti, F.; Mattioli, M. Fibrous zeolites and pulmonary fibroblasts: Toxicological impact and EPR-based insights into cellular alterations. *Environ. Pollut.* **2026**, *397*, 128030. [CrossRef] [PubMed]
21. Hamilton, A.R.; Brook, M.S.; Elangasinghe, A.; Chappell, D.; Patel, J.P.; Kumar, S.; Martin, R. The occurrence and morphology of naturally occurring respirable mordenite mineral fibers in New Zealand. *N. Z. J. Geol. Geophys.* **2026**, *69*, e70056. [CrossRef]
22. Passaglia, E.; Sheppard, R.A. The crystal chemistry of zeolites. In *Natural Zeolites: Occurrence, Properties, Applications*; Bish, D.L., Ming, D.W., Eds.; Reviews in Mineralogy and Geochemistry; Mineralogical Society of America and Geochemical Society: Washington, DC, USA, 2001; Volume 45, pp. 69–116.
23. Utada, M. Zeolites in burial diagenesis and low-grade metamorphic rocks. In *Natural Zeolites: Occurrence, Properties, Applications*; Bish, D.L., Ming, D.W., Eds.; Reviews in Mineralogy and Geochemistry; Mineralogical Society of America and Geochemical Society: Washington, DC, USA, 2001; Volume 45, pp. 277–304.
24. Weisenberger, T.B.; Spürgin, S.; Lahaye, Y. Hydrothermal alteration of the Fohberg phonolite, Kaiserstuhl Volcanic Complex, Germany. *Int. J. Earth Sci.* **2014**, *103*, 2273–2300. [CrossRef]
25. Gottardi, G. The genesis of zeolites. *Eur. J. Mineral.* **1989**, *1*, 479–487. [CrossRef]
26. de' Gennaro, M.; Colella, C. The critical role of temperature in the natural zeolitization of volcanic glass. *Neues Jahrb. Fur Mineral. Monatshefte* **1991**, *8*, 355–362.
27. Hall, A. Zeolitisation of volcaniclastic sediments: The role of temperature and pH. *J. Sediment. Res.* **1998**, *68*, 739–745. [CrossRef]
28. de' Gennaro, M.; Cappelletti, P.; Langella, A.; Perrotta, A.; Scarpati, C. Genesis of zeolites in the Neapolitan Yellow Tuff: Geological, volcanological and mineralogical evidence. *Contrib. Mineral. Petrol.* **2000**, *139*, 17–35. [CrossRef]
29. Novembre, D.; Gimeno, D.; Cappelletti, P.; Graziano, S.F. A case study of zeolitization process Tufo Rosso a Scorie Nere (Vico volcano, Italy): Inferences for a general model. *Eur. J. Mineral.* **2021**, *33*, 315–328. [CrossRef]
30. Mattioli, M.; Cenni, M.; Passaglia, E. Secondary mineral assemblages as indicators of multistage alteration processes in basaltic lava flows: Evidence from the Lessini Mountains, Veneto Volcanic Province, Northern Italy. *Per. Mineral.* **2016**, *85*, 1–24. [CrossRef]
31. Hochella, M.F. *Surface Chemistry, Structure, and Reactivity of Hazardous Mineral Dust*; Health Effects of Mineral Dusts; Reviews in Mineralogy and Geochemistry; Guthrie, G.D., Mossman, B.T., Eds.; Bookcrafters: Chelsea, MI, USA, 1993; Volume 28, pp. 275–308.
32. Lippmann, M. Asbestos exposure indices. *Environ. Res.* **1988**, *46*, 86–106. [CrossRef] [PubMed]
33. Mattioli, M.; Giordani, M.; Dogan, M.; Cangiotti, M.; Avella, G.; Giorgi, R.; Dogan, A.U.; Ottaviani, M.F. Morpho-chemical characterization and surface properties of carcinogenic zeolite fibers. *J. Hazard. Mater.* **2016**, *306*, 140–148. [CrossRef] [PubMed]
34. Cangiotti, M.; Battistelli, M.; Salucci, S.; Falcieri, E.; Mattioli, M.; Giordani, M.; Ottaviani, M.F. Electron paramagnetic resonance and transmission electron microscopy study of the interactions between asbestiform zeolite fibers and model membranes. *J. Toxicol. Environ. Health Part A* **2017**, *80*, 171–187. [CrossRef] [PubMed]
35. Pacella, A.; Fantauzzi, M.; Atzei, D.; Cremisini, C.; Nardi, E.; Montereali, M.R.; Rossi, A.; Ballirano, P. Iron within the erionite cavity and its potential role in inducing its toxicity: Evidences of Fe (III) segregation as extra-framework cation. *Microp. Mes. Mater.* **2017**, *237*, 168–179. [CrossRef]
36. Pacella, A.; Cremisini, C.; Nardi, E.; Montereali, M.R.; Pettiti, I.; Giordani, M.; Mattioli, M.; Ballirano, P. Different erionite species bind iron into the structure: A potential explanation for fibrous erionite toxicity. *Minerals* **2018**, *8*, 36. [CrossRef]
37. Giordani, M.; Mirata, S.; Scarfi, S.; Passalacqua, M.; Fornasini, L.; Drava, G.; Meli, M.A.; Roselli, C.; Mattioli, M. The cyto-toxic/genotoxic role of impurities in soluble minerals: The case of natural (fibrous epsomite) versus synthetic (Epsom salt) magnesium sulphate. *Sci. Total Environ.* **2025**, *966*, 178666. [CrossRef] [PubMed]
38. Gualtieri, A.F.; Bursi Gandolfi, N.; Pollastri, S.; Pollok, K.; Langenhorst, F. Where is iron in erionite? A multidisciplinary study of fibrous erionite-Na from Jersey (Nevada, USA). *Sci. Rep.* **2016**, *6*, 37981. [CrossRef] [PubMed]
39. Pollastri, S.; Gualtieri, A.F.; Gualtieri, M.L.; Hanuskova, M.; Cavallo, A.; Gaudino, G. The Zeta potential of mineral fibers. *J. Hazard. Mater.* **2014**, *276*, 469–479. [CrossRef] [PubMed]
40. Artvinli, M.; Bariş, Y.I. Malignant mesotheliomas in a small village in the Anatolian region of Turkey: An epidemiologic study. *J. Natl. Cancer Inst.* **1979**, *63*, 17–22. [CrossRef] [PubMed]
41. Bariş, Y.I.; Şahin, A.A.; Özesmi, M.; Kerse, I.; Özen, E.; Kolacan, B.; Altinörs, M.; Göktepeli, A. An outbreak of pleural mesothelioma and chronic fibrosing pleurisy in the village of Karain/Ürgüp in Anatolia. *Thorax* **1978**, *33*, 181–192. [CrossRef] [PubMed]
42. Bariş, Y.I.; Artvinli, M.; Şahin, A.A. Environmental mesothelioma in Turkey. *Ann. N. Y. Acad. Sci.* **1979**, *330*, 423–432. [CrossRef] [PubMed]
43. Baris, I.; Artvinli, M.; Saracci, R.; Simonato, L.; Pooley, F.; Skidmore, J.; Wagner, C. Epidemiological and environmental evidence of the health effects of exposure to erionite fibers: A four-year study in the Cappadocian region of Turkey. *Int. J. Cancer* **1987**, *39*, 10–17. [CrossRef] [PubMed]

44. Bariş, Y.I.; Grandjean, P. Prospective study of mesothelioma mortality in Turkish villages with exposure to fibrous zeolite. *J. Natl. Cancer Inst.* **2006**, *98*, 414–417. [CrossRef] [PubMed]
45. Metintaş, M.; Hillerdal, G.; Metintaş, S.; Dumortier, P. Malignant mesothelioma due to environmental exposure to erionite: Follow-up of a Turkish emigrant cohort. *Eur. Respir. J.* **1999**, *13*, 523–526. [CrossRef] [PubMed]
46. Emri, S.; Demir, A.; Dogan, M.; Akay, H.; Bozkurt, B.; Carbone, M.; Baris, I. Lung diseases due to environmental exposures to erionite and asbestos in Turkey. *Toxicol. Lett.* **2002**, *127*, 251–257. [CrossRef] [PubMed]
47. Dogan, A.U.; Baris, Y.I.; Dogan, M.; Emri, S.; Steele, I.; Elmishad, A.G.; Carbone, M. Genetic predisposition to fiber carcinogenesis causes a mesothelioma epidemic in Turkey. *Cancer Res.* **2006**, *66*, 5063–5068. [CrossRef] [PubMed]
48. Carbone, M.; Emri, S.; Dogan, A.U.; Steele, I.; Tuncer, M.; Pass, H.I.; Baris, Y.I. A mesothelioma epidemic in Cappadocia: Scientific developments and unexpected social outcomes. *Nat. Rev. Cancer* **2007**, *7*, 147–154. [CrossRef] [PubMed]
49. Dogan, A.U.; Dogan, M.; Hoskins, J.A. Erionite series minerals: Mineralogical and carcinogenic properties. *Environ. Geochem. Heal.* **2008**, *30*, 367–381. [CrossRef] [PubMed]
50. Giacobbe, C.; Moliterni, A.; Di Giuseppe, D.; Malferrari, D.; Wright, J.P.; Mattioli, M.; Raneri, S.; Giannini, C.; Fornasini, L.; Mugnaioli, E.; et al. The crystal structure of the killer fiber erionite from Tuzköy (Cappadocia, Turkey). *IUCrJ* **2023**, *10*, 397–410. [CrossRef] [PubMed]
51. Carbone, M.; Baris, Y.I.; Bertino, P.; Brass, B.; Comertpay, S.; Dogan, A.U.; Gaudino, G.; Jube, S.; Kanodia, S.; Partridge, C.R.; et al. Erionite exposure in North Dakota and Turkish villages with mesothelioma. *Proc. Natl. Acad. Sci. USA* **2011**, *108*, 13618–13623. [CrossRef] [PubMed]
52. Ortega-Guerrero, M.A.; Carrasco-Núñez, G. Environmental occurrence, origin, physical and geochemical properties, and carcinogenic potential of erionite near San Miguel de Allende, Mexico. *Environ. Geochem. Health* **2014**, *36*, 517–529. [CrossRef] [PubMed]
53. Saini-Eidukat, B.; Triplett, J.W. Erionite and offretite from the Killdeer Mountains, Dunn County, North Dakota, U.S.A. *Am. Mineral.* **2014**, *99*, 8–15. [CrossRef] [PubMed]
54. Van Gosen, B.S.; Blitz, T.A.; Plumlee, G.S.; Meeker, G.P.; Pierson, M.P. Geologic occurrences of erionite in the United States: An emerging national public health concern for respiratory disease. *Environ. Geochem. Health* **2013**, *35*, 419–430. [CrossRef] [PubMed]
55. Patel, J.P.; Brook, M.S.; Kah, M.; Hamilton, A. Global geological occurrence and character of the carcinogenic zeolite mineral, erionite: A review. *Front. Chem.* **2022**, *10*, 1066565. [CrossRef] [PubMed]
56. Patel, J.P.; Brook, M.S.; Kah, M.; Hamilton, A.; Gamberini, M.C.; Zoboli, C.; Mugnaioli, E.; Malferrari, D.; Fantini, R.; Arletti, R.; et al. Characterization and potential toxicity of asbestiform erionite from Gawler Downs, New Zealand. *Am. Mineral.* **2024**, *109*, 1499–1512. [CrossRef]
57. Passaglia, E.; Galli, E.; Rinaldi, R. Levynes and erionites from Sardinia, Italy. *Contrib. Mineral. Petrol.* **1974**, *43*, 253–259. [CrossRef]
58. Pongiluppi, D.; Passaglia, E.; Galli, E. Su alcune zeoliti della Sardegna. *Rend. Soc. Ital. Mineral. Petrol.* **1974**, *30*, 77–100.
59. Giovagnoli, L.; Boscardin, M. Ritrovamento di levyna ed erionite a Montecchio Maggiore (Vicenza). *Riv. Mineral. Ital.* **1979**, *1*, 44–45.
60. Passaglia, E.; Tagliavini, A. Erionite from Faedo, Colli Euganei, Italy. *Neues Jahrb. Mineral. Monatsh.* **1995**, *4*, 185–191.
61. Giordani, M.; Mattioli, M.; Ballirano, P.; Pacella, A.; Cenni, M.; Boscardin, M.; Valentini, L. Geological occurrence, mineralogical characterization, and risk assessment of potentially carcinogenic erionite in Italy. *J. Toxicol. Environ. Health Part B* **2017**, *20*, 81–103. [CrossRef] [PubMed]
62. Mattioli, M.; Giordani, M.; Ballirano, P.; Salvioli-Mariani, E.; Bernardini, S.; Della Ventura, G. First occurrence, crystal-chemistry and structure of erionite, a carcinogenic fibrous zeolite, from the volcanic rocks of Latium (Italy). *Per. Mineral.* **2023**, *92*, 159–178. [CrossRef] [PubMed]
63. Gottardi, G.; Galli, E. *Natural Zeolites*; Springer: Berlin/Heidelberg, Germany, 1985; p. 409.
64. Baerlocher, C.; McCusker, L.B.; Olson, D.H. *Atlas of Zeolite Framework Types*, 5th ed.; Elsevier: London, UK, 2001; p. 398.
65. Coombs, D.S.; Alberti, A.; Armbruster, T.; Artioli, G.; Colella, C.; Galli, E.; Grice, J.D.; Liebau, F.; Mandarino, J.A.; Minato, H.; et al. Recommended nomenclature for zeolite minerals; report of the Subcommittee on Zeolites of the International Mineralogical Association, Commission on New Minerals and Mineral Names. *Can. Mineral.* **1997**, *35*, 1571–1606.
66. Alberti, A.; Martucci, A.; Galli, E.; Vezzalini, G. A reexamination of the crystal structure of erionite. *Zeolites* **1997**, *19*, 349–352. [CrossRef]
67. Bish, D.L.; Ming, D.W. *Natural Zeolites: Occurrence, Properties, Applications*; Reviews in Mineralogy and Geochemistry 45; Mineralogical Society of America: Chantilly, VA, USA, 2001; Volume 45, 662p.
68. Cametti, G.; Pacella, A.; Mura, F.; Rossi, M.; Ballirano, P. New morphological, chemical, and structural data of woolly erionite-Na from Durkee, Oregon, U.S.A. *Am. Mineral.* **2013**, *98*, 2155–2163. [CrossRef]
69. Deer, W.A.; Howie, R.A.; Wise, W.S.; Zussman, J. *Rock-Forming Minerals, Volume 4B: Framework Silicates: Silica Minerals, Feldspathoids and the Zeolites*, 2nd ed.; Geological Society: London, UK, 2004.

70. Gualtieri, A.F.; Artioli, G.; Passaglia, E.; Bigi, S.; Viani, A.; Hanson, J.C. Crystal structure-crystal chemistry relationships in the zeolites erionite and offretite. *Am. Mineral.* **1998**, *83*, 590–606. [CrossRef]
71. Staples, L.W.; Gard, J.A. The fibrous zeolite erionite: Its occurrence, unit cell, and structure. *Mineral. Mag.* **1959**, *32*, 261–281. [CrossRef]
72. Sheppard, R.A.; Gude, A.J., III. Chemical composition and physical properties of the related zeolites offretite and erionite. *Am. Mineral.* **1969**, *54*, 875–886.
73. Gude, A.J., III; Sheppard, R.A. Woolly erionite from the Reese River zeolite deposit, Lander County, Nevada, and its relationship to other erionites. *Clays Clay Miner.* **1981**, *29*, 378–384. [CrossRef]
74. Dogan, A.U.; Dogan, M. Re-evaluation and re-classification of erionite series minerals. *Environ. Geochem. Health* **2008**, *30*, 355–366. [CrossRef] [PubMed]
75. Ballirano, P.; Andreozzi, G.B.; Dogan, M.; Dogan, A.U. Crystal structure and iron topochemistry of erionite-K from Rome, Oregon, U.S.A. *Am. Mineral.* **2009**, *94*, 1262–1270. [CrossRef]
76. Passaglia, E.; Artioli, G.; Gualtieri, A. Crystal chemistry of the zeolites erionite and offretite. *Am. Mineral.* **1998**, *83*, 577–589. [CrossRef]
77. Patel, J.P.; Brook, M.S.; Hamilton, A.; Kah, M.; Mugnaioli, E.; Gualtieri, A.F. Occurrence, crystal chemistry and morphology of erionite from New Zealand. *Min. Mag.* **2026**, *90*, 445–466. [CrossRef]
78. Eakle, A.S. Erionite, a new zeolite. *Am. J. Sci.* **1898**, *s4-6*, 66–68. [CrossRef]
79. Scarfi, S.; Almonti, V.; Mirata, S.; Passalacqua, M.; Vernazza, S.; Patel, J.P.; Brook, M.; Hamilton, A.; Kah, M.; Gualtieri, A.F. In vitro cyto- and geno-toxicity of asbestiform erionite from New Zealand. *Environ. Res.* **2025**, *265*, 120415. [CrossRef] [PubMed]
80. Peccerillo, A.; Conticelli, S.; Manetti, P. Petrological characteristics and the genesis of the recent magmatism of the Southern Tuscany and Northern Latium. *Per. Mineral.* **1987**, *56*, 157–172.
81. Carminati, E.; Lustrino, M.; Doglioni, C. Geodynamic evolution of the central and western Mediterranean: Tectonics vs. igneous petrology constraints. *Tectonophysics* **2012**, *579*, 173–192. [CrossRef]
82. Perini, G.; Francalanci, L.; Davidson, J.P.; Conticelli, S. Evolution and genesis of magmas from Vico volcano, Central Italy: Multiple differentiation pathways and variable parental magmas. *J. Petrol.* **2004**, *45*, 139–182. [CrossRef]
83. Conticelli, S.; Melluso, L.; Perini, G.; Avanzinelli, R.; Boari, E. Petrologic, geochemical and isotopic characteristics of potassic and ultrapotassic magmatism in Central-Southern Italy: Inferences on its genesis and on the nature of mantle sources. *Per. Mineral.* **2004**, *73*, 135–164.
84. Conticelli, S.; Avanzinelli, R.; Poli, G.; Braschi, E.; Giordano, G. Shift from lamproite-like to leucititic rocks: Sr-Nd-Pb isotope data from the Monte Cimino volcanic complex vs. the Vico stratovolcano, Central Italy. *Chem. Geol.* **2013**, *353*, 246–266. [CrossRef]
85. Nappi, G.; Renzulli, A.; Santi, P.; Gillot, P.Y. Geological evolution and geochronology of the Vulsinian Volcanic District (Central Italy). *Boll. Soc. Geol. Ital.* **1995**, *114*, 599–613.
86. Sottili, G.; Trigila, R. Integrated approach for the reconstruction of stratigraphy and geology of Quaternary volcanic terrains: An application to the Vulsini Volcanoes (central Italy). In *Stratigraphy and Geology in Volcanic Areas*; Groppelli, G., Viereck-Goette, L., Eds.; The Geological Society of America: Boulder, CO, USA, 2010; Volume 464, pp. 66–84.
87. Sparks, R.S.J. Stratigraphy and geology of the ignimbrites of the Vulsini Volcano, Central Italy. *Geol. Rundsch.* **1975**, *64*, 497–523. [CrossRef]
88. Palladino, D.; Agosta, E. Pumice fall deposits of the Western Vulsini Volcanoes (Central Italy). *J. Volcanol. Geotherm. Res.* **1997**, *78*, 77–102. [CrossRef]
89. de' Gennaro, M.; Franco, E.; Rossi, M.; Langella, A.; Ronca, A. Epigenetic minerals in the volcaniclastic deposits from central southern Italy: A contribution to zeolite genesis. In *The Volcaniclastic Rocks of Campania (Southern Italy): Special Issue of the Proceedings of the Academy of Physical and Mathematical Sciences of Naples*; Di Girolamo, P., Ed.; Società Nazionale di Scienze, Lettere e Arti in Napoli: Napoli, Italy, 1987; pp. 107–131.
90. de' Gennaro, R.; Cappelletti, P.; Cerri, G.; De' Gennaro, M.; Dondi, M.; Langella, A. Neapolitan Yellow Tuff as raw material for lightweight aggregates in lightweight structural concrete production. *Appl. Clay Sci.* **2005**, *28*, 309–319. [CrossRef]
91. Mattioli, M.; Giordani, M. Post-Emplacement Zeolitization in Ignimbrites: Insights from Central Italy Volcanic Rocks. *Minerals* **2025**, *15*, 924. [CrossRef]
92. Passaglia, E. The crystal chemistry of chabazites. *Am. Mineral.* **1970**, *55*, 1278–1301.
93. Passaglia, E.; Tagliavini, A.; Vezzalini, G. The crystal chemistry of erionite. *Eur. J. Mineral.* **1998**, *10*, 417–426.
94. Ballirano, P.; Pacella, A.; Andreozzi, G.B.; Dogan, M.; Dogan, A.U. Crystal chemical and structural characterization of fibrous erionite. *Minerals* **2017**, *7*, 16. [CrossRef]
95. Aust, A.E.; Cook, P.M.; Dodson, R.F. Morphological and chemical mechanisms of elongated mineral particle toxicities. *J. Toxicol. Environ. Health Part B Crit. Rev.* **2011**, *14*, 40–75. [CrossRef] [PubMed]
96. Seyfried, W.E., Jr.; Bischoff, J.L. Low temperature basalt alteration by sea water: An experimental study at 70 °C and 150 °C. *Geochim. Cosmochim. Acta* **1979**, *43*, 1937–1947. [CrossRef]

97. Gianelli, G.; Teklemariam, M.; Ruggieri, G.; Battaglia, S. Water-rock interaction and hydrothermal mineral equilibria in the Tendaho geothermal system. *J. Volcanol. Geotherm. Res.* **1998**, *86*, 253–276. [CrossRef]
98. Bloise, A.; Barca, D.; Gualtieri, A.F.; Pollastri, S.; Belluso, E. Trace elements in hazardous mineral fibers. *Environ. Pollut.* **2016**, *216*, 314–323. [CrossRef] [PubMed]
99. Pollastri, S.; D'Acapito, F.; Trapananti, A.; Colantoni, I.; Andreozzi, G.B.; Gualtieri, A.F. The chemical environment of iron in mineral fibers: A combined X-ray absorption and Mössbauer spectroscopic study. *J. Hazard. Mater.* **2015**, *298*, 282–293. [CrossRef] [PubMed]
100. Erdem, E.; Karapinar, N.; Donat, R. The removal of heavy metal cations by natural zeolites. *J. Colloid Interface Sci.* **2004**, *280*, 309–314. [CrossRef] [PubMed]
101. de Gennaro, B.; Aprea, P.; Liguori, B.; Galzerano, B.; Peluso, A.; Caputo, D. Zeolite-rich composite materials for environmental remediation: Arsenic removal from water. *Appl. Sci.* **2020**, *10*, 6939. [CrossRef]
102. Fukuda, H.; Ebara, M.; Yamada, H.; Arimoto, M.; Okabe, S.; Obu, M.; Yoshikawa, M.; Sugiura, N.; Saisho, H. Trace elements and cancer. *Jpn. Med. Assoc. J.* **2004**, *47*, 391–395.
103. Fubini, B. The possible role of surface chemistry in the toxicity of inhaled fibers. In *Fiber Toxicology*; Warheit, D.B., Ed.; Academic Press: San Diego, CA, USA, 1993; Volume 11, pp. 229–257.

Disclaimer/Publisher's Note: The statements, opinions and data contained in all publications are solely those of the individual author(s) and contributor(s) and not of MDPI and/or the editor(s). MDPI and/or the editor(s) disclaim responsibility for any injury to people or property resulting from any ideas, methods, instructions or products referred to in the content.